1   **Title Page**

2

3   **Names of the authors:**

4   Pivetta T. (1), Braitenberg C. (1), Barbolla D.F. (2)

5

6   **Title:**

7   Geophysical challenges for future satellite gravity missions: assessing the impact of MOCASS
8   mission

9

10   **Affiliations of the authors:**

11   (1) Department of Mathematics and Geosciences, University of Trieste, Italy
12   (2) Department of Science and Technology of Biology and Environment, University of Salento,
13   Lecce, Italy

14

15   **Corresponding author:**

16   Carla Braitenberg. Email: berg@units.it

17

18   **ORCID Codes:**

19   Tommaso Pivetta: https://orcid.org/0000-0002-8836-8162

20   Carla Braitenberg: https://orcid.org/0000-0001-7277-816X

21   Dora Francesca Barbolla: https://orcid.org/0000-0002-1876-7555

22
23   **Acknowledgments**

30

31
32

Geophysical challenges for future satellite gravity missions: assessing the impact of MOCASS mission

Pivetta T. (1), Braitenberg C. (1), Barbolla D.F. (2)

(1) Department of Mathematics and Geosciences, University of Trieste, Italy

(2) Department of Science and Technology of Biology and Environment, University of Salento, Lecce, Italy

Abstract

The GRACE/GRACE-FO satellites have observed large scale mass changes, contributing to the mass budget calculation of the hydro-and cryosphere. The scale of the observable mass changes must be in the order of 300 km or bigger to be resolved. Smaller scale glaciers and hydrologic basins significantly contribute to the closure of the water mass balance, but are not detected with the present spatial resolution of the satellite. The challenge of future satellite gravity missions is to fill this gap, providing higher temporal and spatial resolution. We assess the impact of a geodetic satellite mission carrying on board a cold atom interferometric gradiometer (MOCASS: Mass Observation with Cold Atom Sensors in Space) on the resolution of simulated geophysical phenomena, considering mass changes in the hydrosphere and cryosphere. Moreover, we consider mass redistributions due to seamounts and tectonic movements, belonging to the solid earth processes. The MOCASS type satellite is able to recover 50% smaller deglaciation rates over a mountain range as the High Mountains of Asia compared to GRACE, and to detect the mass of 60% of the cumulative number of glaciers, an improvement respect to GRACE which detects less than 20% in the same area. For seamounts a significantly smaller mass eruption could be detected with respect to GRACE, reaching a level of mass detection of a submarine basalt eruption of 1.6×10^9 m^3 . This mass corresponds to the eruption of Mount Saint Helens. The simulations demonstrate that a MOCASS type mission would significantly improve the resolution of mass changes respect to existing geodetic satellite missions.

1. Introduction

Variations of the gravity acceleration on the Earth surface occur on a wide spectrum of time and spatial scales. The complementary gravity missions GOCE (Floberghagen et al. 2011) and GRACE and GRACE Follow On (GRACE/FO) (Tapley et al. 2019), successfully mapped the static gravity field and its time variations, giving a data set for delineating geologic structures of interest and mapping subsurface mass variations globally. The static field was obtained from GOCE with high spatial resolution and the dynamic field from GRACE/FO has lower spatial resolution but high sensitivity.

For instance, water movements in wide inland basins, as the Amazonas (S.-C. Han et al. 2010), as well as over the oceans (Jeon et al. 2018) and glaciers (Zemp et al. 2019) were successfully detected and studied from the time variation of GRACE data: the analysis revealed the presence of both periodic annual components and long term gravity trends connected to the underground water flow (Döll et al. 2014). GRACE and GOCE satellites were also able to observe the gravity field variations due to the co-seismic and post-seismic deformations of large earthquakes, such as the Sumatra-Andaman (S.-C. Han 2006) earthquake or the Tohoku event (Cambiotti 2020; S. -C. Han et al. 2015). Plurennial trends in the gravity field variations have been recorded and studied in the Himalaya region (Braitenberg and Shum 2017; Matsuo and Heki 2010; Sun et al. 2009) and interpreted as due to the combination of hydrologic, isostatic and tectonic effects.

Cross continent correlation of the geologic structures is now possible (Braitenberg 2015; Köther et al. 2012) due to the homogenous coverage of observations and the overcoming of geodetic issues that affect the terrestrial measurements. Typically, the problems were connected to the difference in the geodetic reference systems between countries that caused bias at long wavelengths.

The satellite observations from GRACE of the gravity changes have been validated with terrestrial superconducting gravimeters and have shown the complimentarity between terrestrial and satellite observation from GRACE (Abe et al. 2012; Weise et al. 2009, 2012).

These past satellite missions employed a combination of electrostatic accelerometers, which recorded both inertial and gravitational accelerations; the GNSS tracking of the satellite allowed removing the inertial components unveiling the pure gravity attractions. Recently, the advent of Cold Atom Interferometry (CAI) (Carraz et al. 2014; Ménoret et al. 2018), which offers better noise

93   performance with respect to the electrostatic accelerometers, opened a new era for the satellite
94   observations pushing forward the possibilities to monitor geophysical phenomena at smaller scales.

95   A feasibility study of a new satellite mission concept utilizing a CAI sensor, instead of the classic
96   electrostatic accelerometers, was the subject of a project that involved Politecnico di Milano,
97   University of Firenze, University of Trieste and that was funded by the Italian Space Agency (ASI).

98   In the frame of this project, named MOCASS, the three groups analyzed three different aspects of
99   the mission: the University of Firenze studied and defined the characteristics of the instrument for
100 a satellite mission; the Politecnico di Milano performed the mission simulations producing curve
101 errors while the University of Trieste group assessed the possible scientific impact.

102 An overview of the group activities and the overall results has been already published by Migliaccio
103 et al. (2019). In the present work we aim to give more details on the geophysical impact of the
104 mission, presenting in more detail the simulations conducted and some more examples not
105 discussed by Migliaccio et al. (2019). A companion paper to this (Reguzzoni et al. 2021), details the
106 geodetic aspects presenting the simulations of the mission.

107 We are interested in assessing the magnitude of the gravity signals induced by the redistribution of
108 mass due to hydrological, glaciological and tectonic effects.

109 We will focus on the High Mountains of Asia area in particular, which is the world largest Mid
110 Latitude glacierized region and is experiencing an important deglaciation (Gardner et al. 2013). In
111 addition to this, the area is characterized by an intense tectonic activity, along the Main Himalayan
112 Thrust, that is responsible of an uplift of the frontal chain and to significant hydrologic variations.

113

2. Data and Methods

115 The area selected for the simulations is in Central Asia and comprises the High Mountainous of Asia
116 (HMA) region, including the Himalaya and the Tibet plateau, and part of the Indian Ocean. The HMA
117 region constitutes an important system of the earth where several climatic and geodynamic
118 phenomena take place and influence each other. Such phenomena concur in generating huge mass
119 movements, which involve different spatial and temporal scales. In our simulations we will focus on
120 glacial mass variations, crustal deformation due to tectonic processes, hydrology and volcanic
121 eruptions associated to seamounts. All these phenomena generate mass changes and hence gravity

122   signals over a wide spectrum of temporal and spatial scales: from daily-weekly temporal scales for

123   the volcanic activity to long period trends in which the tectonic and climatic signals superpose.

124   For estimating the gravity effects, some constraints on the spatial distribution of the volume and

125   density temporal variations are required. We derived most of them from publicly available

126   databases which are presented in detail in the following.

127

128   **2.1 Glaciers mass variations**

129   For what concerns the estimate of the glacial effect we focus on the HMA system (Gardner et al.

130   2013), which comprises the Himalaya, the Tibet and the northern part of the Himalaya chain (Tien

131   Shan). This orogeny is the greatest worldwide in terms of glaciers surface (118200 km^2) and is

132   currently losing glacial masses at a rate of 220 $kg/m^2/yr$ (Gardner et al. 2013). Glaciers in the region

133   have been studied from combination of satellite products including satellite imagery and previous

134   gravity mission as GRACE. GRACE offered constraints on mass fluxes and these data have been used

135   to provide estimates of the deglaciation as testified by the studies of Matsuo and Heki (2010) and

136   Jacob et al. (2012).

137   In order to construct realistic synthetic models and simulate the gravity change we need constraints

138   regarding:

139   1) The outline of the glaciers

140   2) The yearly rate of change (dh/dt) of the glacier thickness

141   3) A DEM (Digital Elevation Model) model to extract the height information of where the

142   glaciers are located

143   For the outline of the glaciers we rely on the Randolph Glacier Inventory (RGI) (Pfeffer et al. 2014)

144   which is a worldwide database of the glaciers. The database is continuously updated and it is

145   distributed in a shape file that contains the polygons of the outlines and the relative attribute table.

146   The polygons have been extracted mainly from the satellite missions such as Landsat or ASTER

147   (Pfeffer et al. 2014) through automatic algorithms. For many glaciers there are more than one

148   outline, which refer to different times of analysis; using a GIS software we extracted the polygons

149   pertaining on a specific time. From the Randolph catalog we extracted the outlines of the glaciers

150   for the whole Himalaya-Tibet area, following the macro-areas outlined in red in Figure 1a.

151   The yearly rate of change (dh/dt) of the glacier thickness is derived from the study of Gardner et al.

152   (2013), which evaluated the contribution of the deglaciation to the sea level rise, and provided a

153   detailed analysis of the worldwide ice masses variations. In this study the authors gave an estimation

154   of the yearly elevation change (dh/dt) of the glaciers in the Himalaya region, by analyzing the data

155   from IceSat for the period 2003-2009. The authors reported the average dh/dt values for the macro-

156   regions of the RGI catalog shown in Figure 1a. In the same figure the glaciers outlines are colorized

157   with a color scale proportional to the deglaciation rate of (2013). Blue values show high deglaciation

158   rates dh/dt> 0.5 m/yr, yellowish colors show stable glacial thicknesses, while red values, which are

159   found only in one sector of the western Tibet, report glacial thickening.

160   The last constraint is the DEM model, which is necessary to correctly locate in space the glacial

161   masses. We take advantage of the ETOPO1 model (Amante and Eakins 2009) which offers global

162   topography/bathymetric values at a resolution of 1'.

163

164
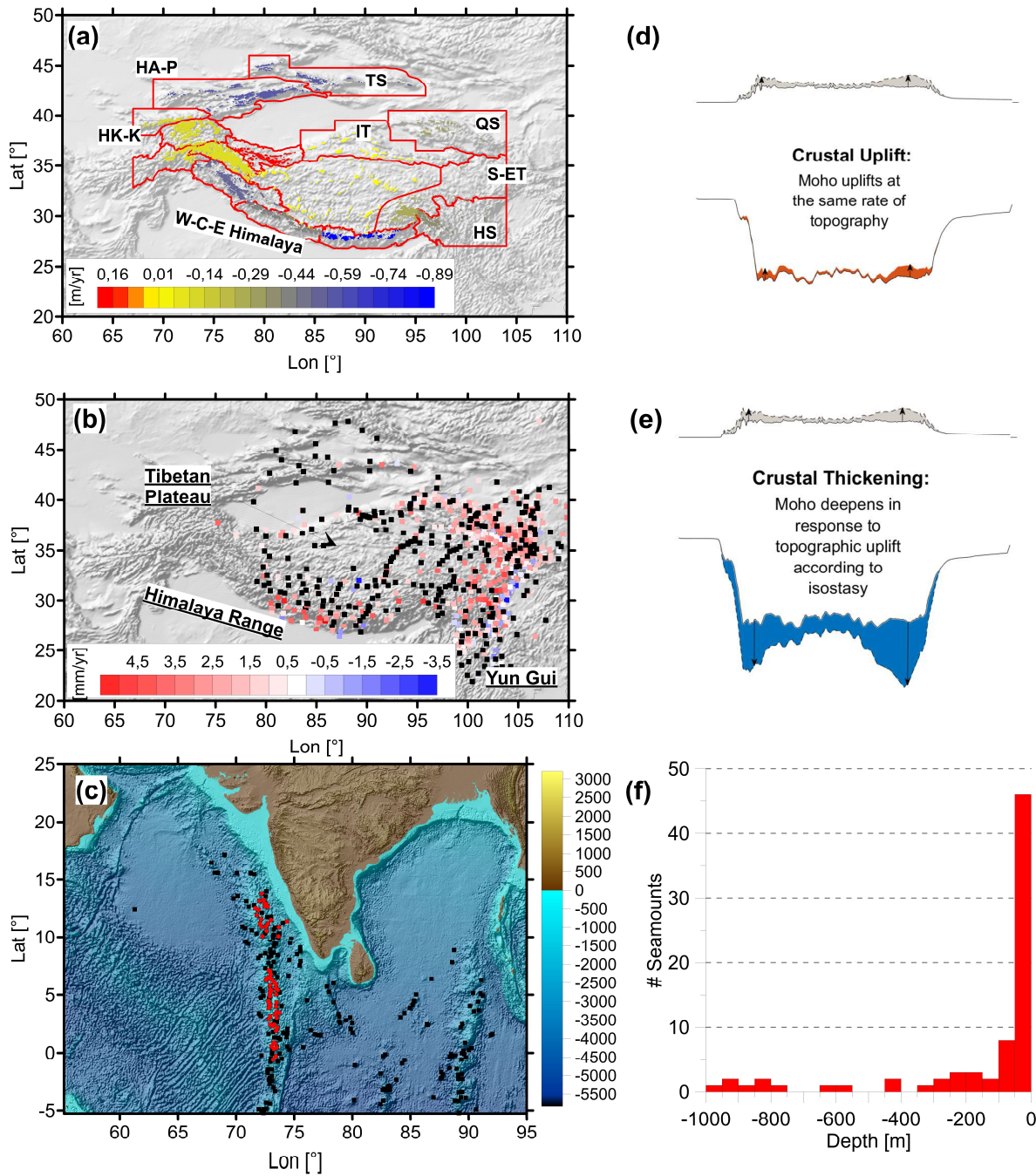
Figure 1. a) outlines of the glaciers in the HMA region according to RGI catalogue (Pfeffer et al.

2014), colorized proportionally to the (de)glaciation rate in m/yr. The sub-regions defined in the RGI

catalogue are outlined in red and labeled with the following acronyms: HA-P: Hissar Alay and Pamir;

TS: Tien Shan; QS: Qilian Shan; S-ET: South and East Tibet; HS: Hengudan Shan; IT: Inner Tibet; W-C-

E Himalaya: West-Central-East Himalaya; HK-K: Hindu Kush and Karakoram. In the background the

ETOPO1 hill-shade map. b) GNSS observations available in the study area; color scale gives the

vertical rates. For black dots only horizontal rates are available and do not enter this study. In the

172 *background the ETOPO1 hill-shade map. c) topo/bathymetry of the area from ETOPO1 with the*

173 *seamounts location according to the Wessel et al.* (2010) *catalogue (black squares) and the*

174 *seamounts with top within 200m from the surface (red points). d) sketch illustrating the crustal uplift*

175 *model. e) model of crustal thickening. f) statistical distribution of the seamounts based on their top's*

176 *depth from sea surface.*

177

178 **2.2 Tectonic deformation and mass movements**

179 The tectonic forces cause horizontal and vertical movements of the lithospheric plates that are

180 captured by the GNSS network data. For example in the Himalayan region the convergence of the

181 Indian and Asian plates, that causes frequent earthquakes, is accommodated by the mountain rising

182 which peaks up to 5mm/yr (Fu and Freymuller, 2012; Liang et al., 2013). This deformation causes

183 mass redistribution and hence a variation in the gravity field. However, such deformation does not

184 involve only the most superficial crustal layers but it also affects deeper crustal units, probably down

185 to the Moho discontinuity.

186 Two end member mechanisms could be hypothesized (Braitenberg and Shum 2017; Chen et al.

187 2018; Yi et al. 2016) as a crustal response to an uplift of the topography:

188   1) the Moho is shifted upwards by the same amount of the topography and the empty space

189   at the base of the crust is filled by the mantle upwelling. This mechanism is equivalent to the

190   crustal response to unloading (Figure 1d)

191   2) the Moho thickens as an isostatic response to the increased topographic load (Figure 1e)

192

193 In order to evaluate the gravity effects of these two models we need as constraints the yearly

194 vertical rates due to the tectonic deformation, and additionally a DEM model. The vertical rates are

195 derived from two published studies (Fu and Freymueller 2012; Liang et al. 2013). Fu and Freymueller

196 (2012) analyzed the GNSS time series data of over 30 stations in the Nepalese area while Liang et

197 al. (2013) used over 750 GNSS stations to represent the current crustal motion and deformation for

198 a wider area including the Tibetan Plateau, Yun Gun and Sichuan regions. Both the studies analyzed

199 continuous GNSS data (Liang et al. 2013 also included some GNSS stations acquired in Campaign

200 mode) and removed the seasonal periodic oscillations obtaining finally the vertical rates adjusting a

201 linear trend. For the Himalaya area, the comparison of the rates along 2D profiles shows that the

202 observed values are compatible in terms of magnitude with those predicted from a simple model of

203 inter-seismic strain accumulation. As we see in Figure 1b the largest vertical rates are observed in

204 the Himalayan range where the uplift easily exceeds 5 mm/yr; the Tibet is generally uplifting as well

205 but at lower rates and with some localized subsidence zones in correspondence of small basins. The

206 zones in the Eastern part of the plateau, are characterized by marked uplift in the northern section,

207 while in the south, towards the Yun Gui plateau, stable terranes or subjected to subsidence are

208 observed.

209

210 **2.3 Large Scale superficial hydrology**

211 The hydrologic effect of the Himalaya region was estimated using the GLDAS (Global land data

212 assimilation systems) products. GLDAS is a project that offers several databases of the land surface

213 state and fluxes in the whole world, at different spatial and temporal resolutions (Rodell et al. 2004).

214 Surface temperature, snow cover, soil moisture, vegetation index are examples of the physical

215 parameters that could be extracted. Each of these is provided at monthly, daily and also 3 h

216 temporal resolutions, while 0.25° and 1° are the spatial resolutions available. The database is

217 constructed incorporating direct observations of the various phenomena from satellite or from

218 ground based observations and modelling procedures. The moisture of the first 2 meters of the

219 ground is one of the available physical parameters offered and the most interesting for our

220 purposes.

221 The moisture database from GLDAS has been already used for correcting geodetic time-series from

222 hydrologic effects: some applications with GRACE could be found in (2010) or for GNSS in Yi et al.

223 (2016). 3 hours resolution models are also largely employed for correcting Superconducting

224 Gravimeter observations (Mikolaj et al. 2016). We exploited the GLDAS soil moisture product for

225 the India-Tibet area, with a spatial resolution of 0.25° and temporal resolution of 1 month. We

226 selected a period for the analysis that spans from 2002 to 2016. The moisture is provided in various

227 NetCDF grids in terms of equivalent water mass in kg per m^2.

228

229 **2.4 Seamount growth**

230 Sea mounts are submarine mountains that are very narrow and very tall, emerging for several

231 thousand meters above the bathymetry. They are formed through volcanism and some are active

232   volcanoes of the ocean floor. A static sea mount bears hazard for shipping when its top reaches

233   shallow depths of about 100m. The international database of seamounts relies greatly on the

234   inversion of the gravity field recovered from satellite altimetry. Models of temporal changes in the

235   gravity field from satellite altimetry are unavailable, and this technique seems to be difficult to be

236   used for generating gravity changes in time. The complete coverage of the gravity changes is not

237   possible with an altimetric satellite placed on a repeat orbit, since the areas between the orbit paths

238   are not monitored. An alternative could be the geodetic gravity satellites, designed for regular

239   observation of the gravity field, although they have a coarser space resolution. The hazard of a

240   seamount is when it grows to a height that could be intercepted by a ship, taking into account the

241   tallest waves that could affect the area during the strongest wind force and ocean state. In this case

242   the relevance of the monitoring is given by the depth distribution of the top of seamounts below

243   the ocean surface, and the resolution of the mass change that adds mass to the top during a growing

244   episode of the seamount. Multispectral satellite images can be used to detect the seamount once

245   it has reached the surface, but the images are not useful in detecting a growing mount before it

246   reaches the surface. We therefore analyze the relevance of catching the signal of a growing sea

247   mount, next to the sensitivity of documenting existing ones.

248   The sensitivity analysis of the gravity signal due to sea mounts is done in the area of the Indian

249   Ocean. Our estimate of the signal of a growing sea mount is not tied to the specific area of the Indian

250   Ocean, but is intended to be an estimate in general terms. Therefore, the question whether

251   specifically in the Indian Ocean the seamounts are volcanically active is beside the point, since we

252   analyze this area due to the large amount of seamounts, generating a reliable statistic. Figure 1c

253   shows with black squares the seamounts distribution according to the database of seamounts

254   compiled by Wessel et al. (2010) in which the seamounts were identified using the ERS-1/Geosat

255   gridded vertical gravity gradient. The database contains longitude and latitude of each seamount,

256   radius and height, and the age of underlying seafloor. Figure 1f shows the statistical distribution of

257   the depths of the tops of the seamounts; we derived the tops depth from the ETOPO1 mode. As it

258   is evident most seamounts have shallow tops, mostly below 100 m.

259   For our scopes we are interested in determining the depth of the top of the seamount with the aim

260   of simulating the eruptions, just imposing different extra volcanic masses on top of it. The volumes

261   of the eruptions tested are derived from estimates of historical eruptions, as we will discuss in the

262   following, and they are in the range of $10^8\,m^3 - 10^9\,m^3$.

263

3. Forward modeling of the gravity fields

For calculating the temporal gravity variations we discretize the masses of the various geophysical phenomena through tesseroids (Uieda et al. 2016) except for the seamounts, in which we exploit a numerical solution of the Poisson equation through a finite element solver. The tesseroids are the equivalent of prisms in a spherical reference system and as the prisms represent a 'building block' through which to build arbitrary complex mass distributions. In order to calculate the gravity effects of glacial thickness variations we select the outlines from the RGI catalogue pertaining to the HMA region and for each outline we extract the topography quotas from the ETOPO1 model (Amante and Eakins 2009). For each topographic point we construct a tesseroid with a basal area of 0.0167° x 0.0167°, matching the ETOPO1 resolution, and a thickness corresponding to the yearly height change of the glacier, according to Gardner et al. (2013). The density of each tesseroid is fixed to be equal to 900 kg/m^3. The yearly mass change per unit area is reported in the supplementary Figure S1a.

The gravity effect of the glaciers for the Himalaya region is calculated on a regular grid of 0.25° resolution at 250 km of quota and it is shown in Figure 2a.
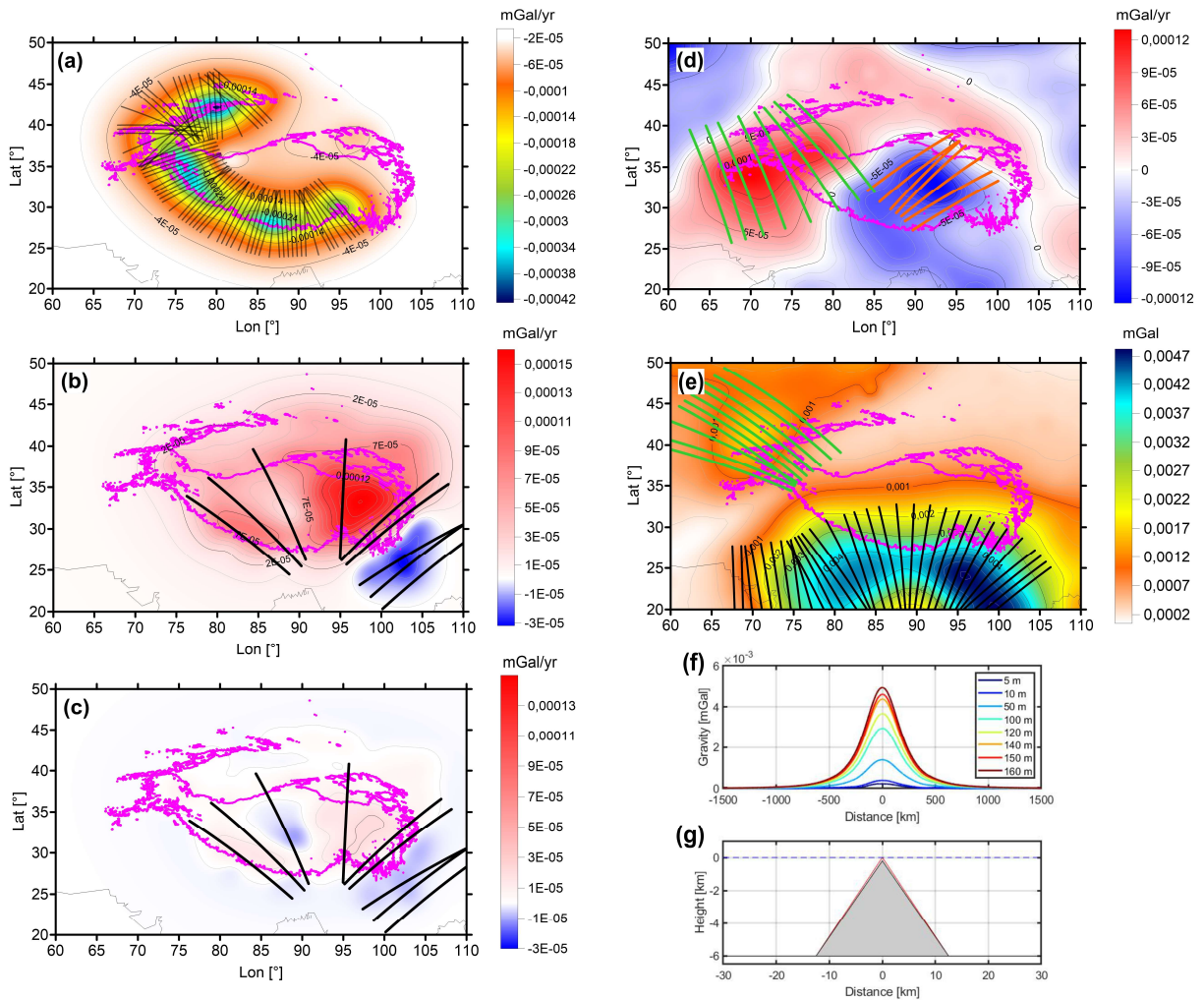
Figure 2. *Simulated gravity fields. a) yearly gravity change due to glaciers thickness variations. b) tectonic yearly gravity change due to crustal uplift. c) yearly gravity change due to an isostatic response of the crust to surface vertical movements. d) hydrologic long period trend from GLDAS. e) annual signal amplitude due to hydrology. In all figures the purple outline reports the 3500 m topographic isoline and black line shows the coastline; the various thick lines that cross the anomalies are the traces of the profiles used for the spectral analysis discussed in the following sections. f) gravity change due to a seamount growth as a function of the maximal thickness of the eruptions. g) cross section of the seamount geometry.*

For the tectonic signals we proceed similarly as for the glacier signal; first we interpolate the sparse GNSS observations over a regular grid of 0.25° resolution for the whole area. We then calculate the gravity contribution of the ETOPO1 topography subjected to the interpolated vertical movements,

12

292   assuming the crustal density ρ_c to be constant and equal to 2670 kg/m³. The mass model is reported

293   in Figure s1b. The crustal response is then assessed according to the models presented previously:

294   in case of a pure crustal uplift the Moho is shifted up by the same amount of the topography and it

295   is replaced by the denser mantle ($\rho_m = 3200$ kg/m³). Conversely when subsidence occurs the Moho

296   is shifted downwards, and light crust now replaces the mantle. In both the situations the signals due

297   to the vertical movements occurring on surface are amplified by the deep crust mass redistribution.

298   In our case the Moho interface in the HMA region is approximated by an isostatic Moho. The signals

299   for the crustal uplift model are shown in Figure 2b.

300   The isostatic response for a surface uplift predicts a lowering of the Moho interface, with sequent

301   increase of the crustal thickness, replacing the dense mantle. Here the superficial mass excess is

302   counter-balanced by a mass loss at the Moho level. Given the densities of the crust and mantle we

303   could calculate the crustal thickness variation Δr for a surface mass variation on topography ($\rho_c \Delta h$)

304   by the following equation:

305

$$\rho_c \Delta h = (\rho_c - \rho_m)\Delta r \tag{1}$$

306

307   The gravity variations associated to the isostatic effect are shown in Figure 2c. We see they are in

308   general one order of magnitude lower than the pure crustal uplift response.

309   The last effect we inspect for the HMA is due to the surficial hydrology which is estimated relying

310   on the monthly GLDAS soil moisture product. Each monthly grid is discretized in tesseroids with

311   resolution equal to that of the model (0.25°) and the gravity effect is calculated at 250 km obtaining

312   a volume of data g_z(lat, lon, time). For each longitude and latitude couple we extract the g_z time

313   series and we fit it with the following equation:

314

$$g(t) = mt + A \sin\left(\frac{2\pi t}{365.25}\right) + B \cos\left(\frac{2\pi t}{365.25}\right) \tag{2}$$

315

316   obtaining a map of the linear trend (m) and of the yearly hydrologic oscillation amplitude defined

317   as $\sqrt{A^2 + B^2}$. Both the long period and seasonal mass changes are reported in Figure S1c and d.

318   Figure 2e shows the periodic annual component in the HMA region; the most prominent signal

319   comes from the Ganges and Brahamputra region, where the yearly signal reaches the 0.004 mGal

320   amplitude. Another interesting periodic signal is observable in the NW region of the map, which

321   corresponds to the Fergana Valley (Uzbekistan).

322   The last Figures 2f and 2g show the simulations of a sea mount eruption and the resulting gravity

323   change. Mechanically the eruption should be a non-explosive magma outflow of basaltic lava at the

324   top, which is immediately cooled by the ocean, analogous to the formation of pillow lavas. We

325   consider a seamount with a cone-like shape of radius 12500 m, height 5800 m, top at 200 m below

326   sea surface, as shown in sketch 2g. We successively add magmatic volume to the top, with an

327   increasing height of 5 m, 10 m, 50 m, 100 m, 120 m, 140 m, 150 m and 160 m. Density of the

328   seamount is 2800 kg/m^3. For each magmatic event the gravity field change is displayed in Figure 2f

329   with color code proportional to the maximal thickness of the eruption.

330   To further prove the goodness of our simulations we compare the summed effects of the tectonic

331   and glacier signals with the yearly gravity trends observed by GRACE. We rely on the Jet Propulsion

332   Laboratory (JPL) monthly solutions synthetised for the period 2002-2016, corrected for the

333   hydrologic component estimated through the GLDAS products. From the various monthly grids we

334   extract the long period trend which is shown in Figure 3a. In the simulated fields (Figure 3b) the high

335   frequency contribution is filtered out through a low-pass Gaussian filter, with cut off wavelength of

336   500 km.

337   From the comparison of the two plots we note a general good agreement both for what concerns

338   the pattern of the anomalies and their amplitudes. For instance, the arch shaped anomaly due to

339   the glaciers is present in both observation and models in the southern part of Tibet and in the

340   Central Himalaya. In the western sector (Lon: 75°; Lat: 30°) GRACE predicts a wider anomaly zone

341   compared to our simulations. This is probably due to a long-term water mass variation associated

342   to intense anthropogenic water extraction (Saji et al. 2020) which is not modelled in GLDAS

343   products. The crustal tectonic uplift seems to be able to explain part of the positive trend in the

344   Central-Eastern Tibet, the mismatch in amplitude could be caused by other components not

345   modelled such as water volume variations associated to the endorheic lakes, as suggested by Zhang

346   et al. (2017).
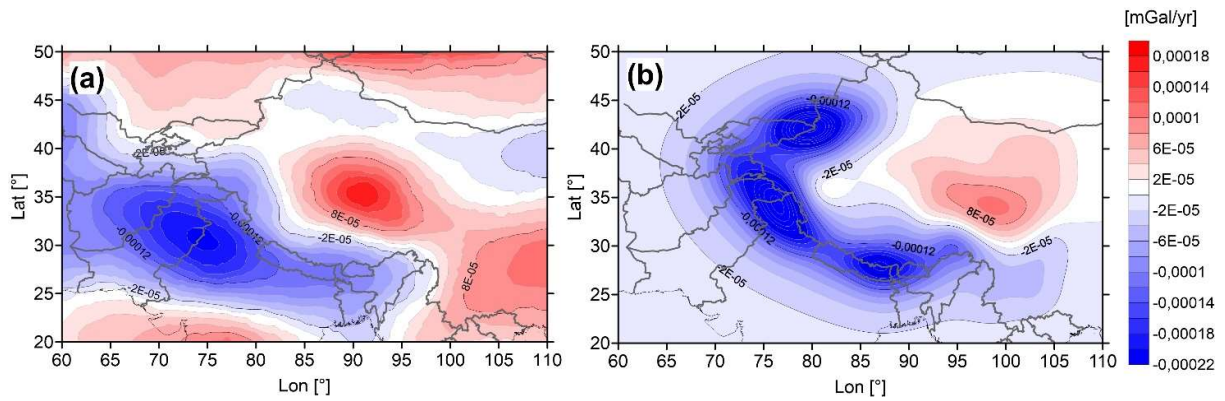
Figure 3. *a) observed long-term yearly gravity rates from GRACE after removing the surface hydrologic component from GLDAS. b) Combined gravity effects of the glaciers and tectonic uplift; the original grids have been low pass filtered removing the spatial frequencies above 1/500 km.*

4. Geophysical Impact assessment

The final step of the research aims at setting the results of the geophysical simulations of the expected gravity field into the context of the error curves of the innovative satellite gravity mission (Migliaccio et al. 2019; Reguzzoni et al. 2021). In order to evaluate the significance of the satellite mission using the atom gravimeter on board, we estimate the percentage improvement of the completeness of phenomena that can be observed. Given a topic of investigation, as for instance detection of the mass loss of a glacier, it is obvious that an increased precision and accuracy of the gravity observation and a higher spatial resolution, allows to detect smaller glaciers loosing minor ice mass due to melting. The question we pose is the significance of the improvement, which is based on the quality jump of the investigations that can be achieved only with the new mission.

One criterion starts from the statistical evaluation of the numerosity-size distribution of the glaciers, or the other phenomena we have investigated (hydrologic basins, sea mounts, mountain dynamics). Given a detection threshold, the percentage of the glaciers that can be monitored is a criterion that we estimate. In the following the results for mountain building process, hydrologic basins, glaciers and sea mounts are discussed.

15

4.1 Time variable phenomena

First, the gravity change of the sum of the glaciers is analyzed. With the scope of comparison with the spectral error curves, it is necessary to determine a gravity change value corresponding to the characteristic wavelength. This is done by tracing a series of orthogonal profiles across the mountain belts, along which the gravity change rate variation is determined. We proceed to estimate the typical wavelength and amplitude of the considered phenomena. For each profile reported in the previous Figure 2 we fitted the following function according to Jekeli (1981):

$$g(x) = b \cdot e^{-a(1-\cos(x))} \tag{3}$$

The function resembles a Gaussian function assuming a >0 and for 0< x <π. Jekeli (1981) reported that a is related to the inverse of the second moment of the Gaussian distribution (σ^2). We estimated the wavelength of the signal to be 4σ; b is the amplitude of the signal. The following Figure 4a reports an example of the fitting procedure over a profile traced on the glacier simulation and the fitted curve from equation 3 (fitting curve in red).

(a)

(b)
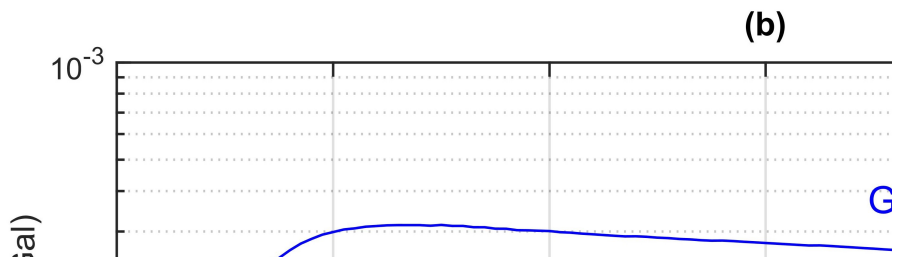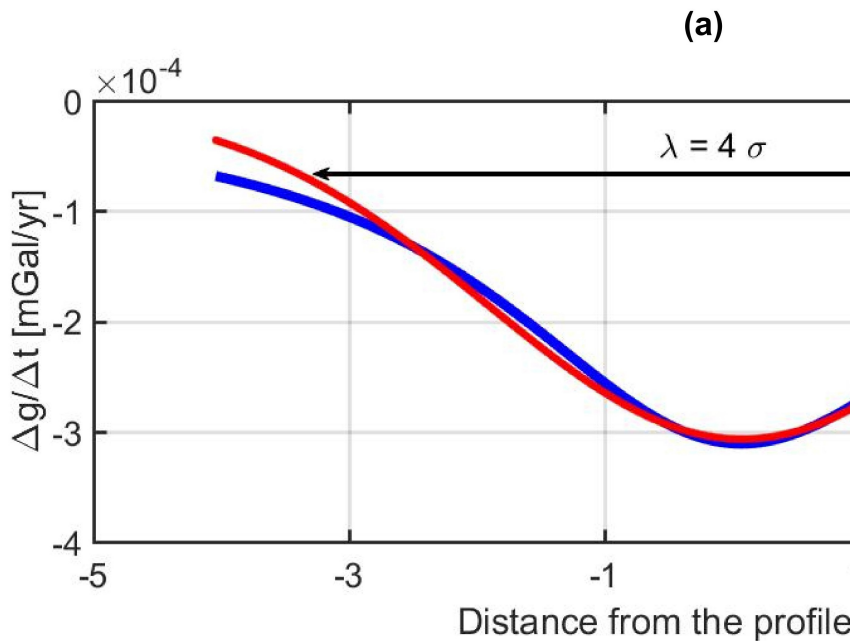
Figure 4. a) red: estimation of typical wavelength and amplitude of a phenomenon given a profile across the anomaly. Blue: observed deglaciation rate in one profile in HMA, red approximated Gaussian curve. b) Spectral comparison of the simulated gravity change of the entire presence of glaciers for the profiles that cross the High Mountain of Asia with the error curves of satellites GRACE, GOCE and MOCASS in two configurations. Each data point (blue dots) corresponds to the signal along one profile (Figure 2a) of the cumulated effect of glaciers. Standard deviations of both amplitudes and degree are plotted with the error bars. Green dots: glaciers signal with a lower deglaciation rate of 50%.

The estimated wavelengths and amplitudes for each profile are reported through dots in the error curves of the mission. A phenomenon can be detected if the signal (dot) lies above the noise curve.

17

In the specific case of the glaciers in Himalaya and the other mountain ranges surrounding the Tibetan plateau, the glaciers are in close proximity, and coalesce to form a broad glacier surface, producing a long wavelength signal. It is a more favorable situation than other areas with single glaciers, as could be the case of the Alps, with a much lower density of glaciers. The wavelength of the signal of a single glacier, approximately a point mass, is large at the height of the satellite, for instance at 250 km, and is in the order of degree 50 in the spherical harmonic expansion. As seen in Figure 4b the present deglaciation is well above the error curves of both MOCASS and GRACE. Of interest is the observation of variations in the average yearly rate, for instance to determine whether recent variations of accelerated deglaciation are visible. Here MOCASS shows to be superior, because it is able to catch lower fluctuation rates (less than 50%; green dots), which instead lie on the error curve of GRACE, and therefore cannot be detected.
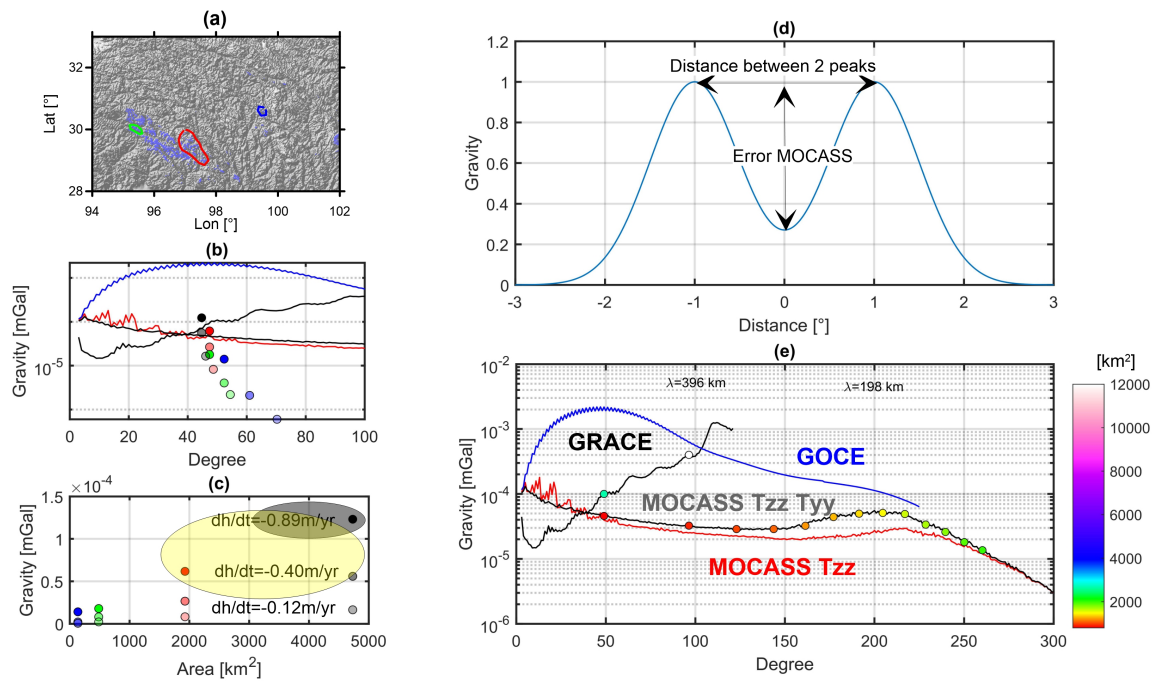
Figure 5. *a) Four classes of glacier areas of increasing areal extent in which glaciers have been aggregated. Outlines mark classes: blue: 100 km², green: 500 km², red: 1900 km², and the total area of the glaciers in the window is 4750 km². In purple the glaciers outlines from RGI. b) Spectral comparison of the simulated gravity change for single glaciers or groups of glaciers in HMA with the error curves of satellites GRACE, GOCE and MOCASS in two configurations. The error curves correspond to one year of gravity observation. c) area of glaciers and the gravity change in one year*

18

413   *due to height loss of the glaciers. Different rates of height loss are assumed (-0.12 m/yr, -0.40 m/yr,*

414   *-0.89 m/yr). The single simulations are compared to the error curves in the plot b of the same figure.*

415   *The gray and yellow areas report the deglaciation rates and glacierized areas sensed by GRACE and*

416   *MOCASS. d)* Minimum distance between two gravity peaks to be distinctly detected. e*) Resolving*

417   *power of MOCASS for distinguishing two adjacent glaciers from their gravity change rate. The dots*

418   *are colored according to their areal extent. Glacial height loss is assumed to be 0.4 m/yr.*

419

420   Next we consider the gravity signal at 250km height due to the changing mass of grouped glaciers

421   of increasing areal extent, imposing three different deglaciation rates (-0.12, -0.40, -0.89 m/yr),

422   which are realistic values derived from Gardner et al. (2013). The characteristic wavelength is found

423   through fitting a Gaussian curve, of which the half width (sigma) is set equal to a fourth of the signal

424   wavelength. The amplitude of the Gaussian curve is taken as the amplitude of the estimated signal

425   at the specific wavelength. We compare this gravity change value with the spectral error curves of

426   three satellites, the GRACE, GOCE and MOCASS in two configurations, estimated for one year of

427   data acquisition. The two MOCASS error curves are for the MOCASS nadir-pointing double-arm

428   configuration, with atomic single-arm or double-arm gradiometer (Migliaccio et al. 2019), at low

429   orbit of 239 km height. The comparison assumes that the mass change of glaciers is steady state, so

430   a yearly sampling of the signal is sufficient. The results are shown in plots 5b and 5c. Due to the

431   calculation height of 250km the wavelength of the signal, also for a small glacier, is relatively large

432   and is in the range of degree 50 and 70. This because the gravity signal also for a point mass widens

433   with increasing height, independently of the diameter of the point mass. The color codes of the dots

434   correspond to four glacier areas, in which smaller glaciers have been gathered to form a compound

435   glacier of increasing size. The four glacier areas are shown in Figure 5a. The glacier areas smaller

436   than 500km^2 are below resolution of the satellites. Starting with an area of 1900 km^2 the

437   deglaciation can be observed, for rates above 0.40 m/yr, but only with MOCASS, not with GRACE.

438   Glaciers as big as 4750 km^2 must have a rate of at least 0.4m/yr to be seen by GRACE, while also

439   smaller rates are detected by MOCASS.

440   A further question is, whether the deglaciation signal of two neighboring glaciers of the HMA can

441   be resolved, and which is the smallest resolvable distance between the glaciers. We estimate this

442   distance by approximating two glaciers by a point mass. The volume change is equal to the area of

443   the glacier times the assumed deglaciation rate of -0.40 m/yr. Given the spectral error value *dg(n)*

444   of the satellite, two glaciers can be resolved if the difference between the gravity of one glacier and

445   the gravity minimum value of the superposition of two glaciers is smaller than the degree error

446   (Figure 5d). The distance between the two peaks of the point masses is the lateral resolution.

447   The distance $dist$ is given by the following equation, with G the gravitational constant, M the yearly

448   mass loss of the two glaciers, h the calculation height, and σ the error at degree n.

449

$$dist = \left(\frac{GMh}{\frac{GM}{h^2} - \sigma(n)} \right)^{3/2} \tag{4}$$

450

451   Given the calculation height and spectral error, and making the area of the glacier vary between

452   500 km^2 and 12000 km^2, we determine the smallest distance between the two glaciers that can be

453   resolved. The deglaciation rate is fixed to 0.40 m/yr (Figure 5e). The smaller glaciers can only be

454   resolved at greater distances. At degree n=50, corresponding to a distance of 792 km, MOCASS

455   resolves two glaciers of about 800 km^2 size, whereas GRACE can resolve two glaciers of more than

456   double size, of about 3000 km^2. At degree n=100, MOCASS resolves glaciers of size 900 km^2, GRACE

457   only glaciers of size 12000 km^2.
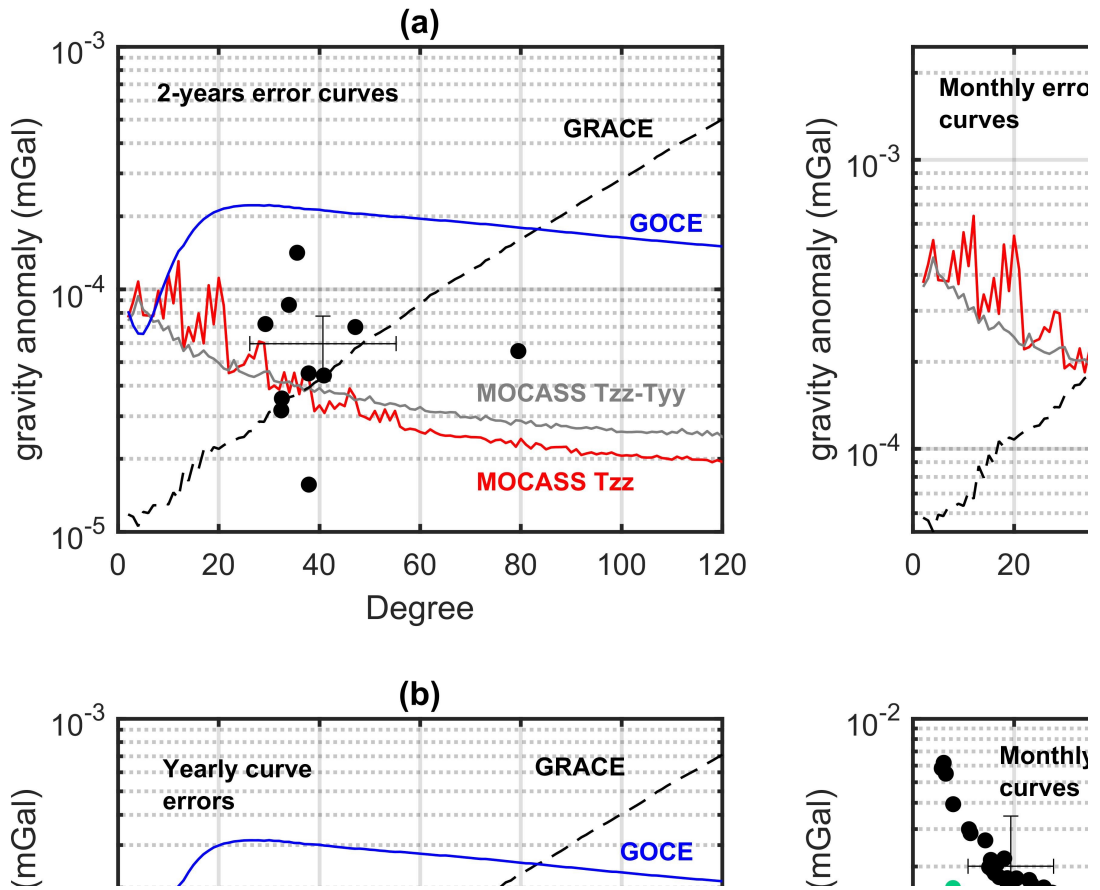
Figure 6. a) Yearly gravity change rate at 250km calculation height for Tibet-Himalaya due to tectonic uplift measured by GPS. The black dots display the characteristic wavelength and amplitude for the profiles in Figure 2b. The satellite error curves are 2-years solutions. b) Hydrologic linear trend in the HMA region at 250 km calculation height. The dots display the characteristic wavelength and amplitude of the signal along the profiles shown in Figure 2d. Green dots are for Pakistan area; red dots are relative to Eastern Tibet. The satellite error curves are 1 year solutions. c) Gravity change at 250 km calculation height for the magmatic growth of a seamount compared to the satellite error curves. The labels report the height increase of the submerged volcanic edifice. Monthly error curves for different satellite missions are shown. d) Hydrologic annual oscillation amplitude in the HMA region at 250 km calculation height. The dots display the characteristic wavelength and amplitude for the profiles shown in Figure 2e. Black dots are for India and Bangladesh area; green dots are relative to Uzbekistan. The satellite error curves are 1-month solutions.

472   Then, we compare the signal amplitudes with the error curves for the other phenomena considered.

473   In all cases the profiles, for which the traces are reported in Figure 2, are fitted with a Gaussian

474   function to find the characteristic wavelength and its amplitude, for comparison with the spectral

475   error curves.

476   We start with the tectonic signals, which are shown in Figure 6a. The greater part of the signal can

477   be resolved both with GRACE and MOCASS, but some features are completely lost in the GRACE

478   observation, as the dot at n=80 which corresponds to a localized subsidence in the North Tibet

479   plateau. To understand the origin of the subsidence, the knowledge of the gravity change rate is

480   necessary, which can be resolved by MOCASS.

481   The hydrologic signals sensitivity is shown in the plots 6b and 6d. In both cases, aperiodic and

482   periodic patterns, two areas are analyzed by fitting a Gaussian curve to the anomaly profiles. For

483   the trends (Figure 6b) we observe that the signals are very close to the error curves; GRACE performs

484   better at low spatial frequencies (low n) while MOCASS, with the flat error curve for $n>40$, detects

485   some high frequency signals that are below the GRACE error curve. This simulation shows the

486   complementarity of the missions; a combined gravity field model including GRACE follow-on and

487   MOCASS could greatly improve the understanding of the dynamics also in small basins.

488   The signal generated by submarine mass variations due to seamount growth sensitivity is plotted in

489   Figure 6c. Major eruptions can be seen both in GOCE and GRACE, but only MOCASS is sensitive to

490   the more realistic eruptions, increasing height by a few meters. In the case we chose, a height

491   increase of 5 m would be seen by MOCASS, whereas GRACE would need an increase of more than

492   10 m. In terms of volumes, for an eruption of 3 m, the erupted volume is $4.9\ 10^8$ m^3, of 5 m, the

493   erupted volume is $8.2\ 10^8$ m^3, and for 10 m, the erupted volume is $1.6\ 10^9$ m^3. These numbers can

494   be compared with the volume erupted with the Saint Helens volcanic eruption, which produced 1.6

495   10^9 m^3 of volume in a single eruption. Our estimate is of first order and could be refined in more

496   detail by including a model of the magmatic production of a sea mount, with the feeder channel

497   from lower crust and mantle and the magma chamber. In the case that the magma system outpours

498   the magma, but is not refilled from below, the mass change would be smaller than we have

499   estimated. Our estimate assumes that the erupted volume is replaced in the magma chamber

500   through rising magma in the feeder channel.

501   Finally, we compare the amplitude and wavelength of the annual signal, calculated over different

502   profiles (traces are reported in figure 2e), with monthly satellite error curves in Figure 6d. The

503 amplitudes and wavelengths of the phenomena have been calculated with the approach already
504 presented in the previous sections.

505 The signals are all well above the noise threshold of both GRACE and MOCASS missions.

506

507 **4.2 Glaciers static detection**

508

509 The final analysis on glaciers regards the problem of total mass detection of a glacier. This is relevant
510 when the area of the glacier has been determined from remote sensing as with SAR and
511 multispectral images, but the thickness is unknown (e.g. for Julian Alps Colucci and Žebre (2016)).
512 In the simulation we calculate the gravity field generated by the ice-mass. It may be argued, that if
513 the glacier surface is known, and the topography erroneously has been set equal to this glacier
514 surface, the glacier mass must be calculated using the density contrast of ice relative to the rock
515 constituting the topography. To make the analysis more general, and assuming the topography
516 represents the bottom surface of the glacier, we use the density contrast of ice against air. In the
517 case that the contrast must be calculated as ice against rock, the gravity signal will be greater by a
518 factor 1.6. This because the density of ice is close to 1000 kg/m^3, the density contrast of ice against
519 rock is -1600 kg/m^3, assuming a granite rock density of 2600 kg/m^3. We calculate the glacier volume
520 starting from the areal extent using an empirical formula for the glacier height (Bahr et al. 2015),
521 with S the area in km^2 and V the volume in km^3:

$$V = 0.03 S^{1.36}$$

(5)

522 Single glaciers of different size are selected for the HMA from the Randolph database, and
523 discretized into tesseroids of 1' sides. The base of the tesseroids is set equal to the ETOPO1
524 topographic height, the top is calculated through the empirical height formula. Gravity calculation
525 height is 10 km, so as to be above the topography. Only for the smallest area of 10 km^2 a single
526 tesseroid of square footprint is used. Again the signal is fit with a Gaussian curve to determine
527 wavelength and amplitude, and these values are compared to the 5 yr error curves of the satellites.
528 Approximately the observation thresholds are a glacier area of 250 km^2 for GRACE, 100 km^2 for
529 GOCE, and 10 km^2 for MOCASS, as seen in Figure 7.

(a)

(b)

(c)

530
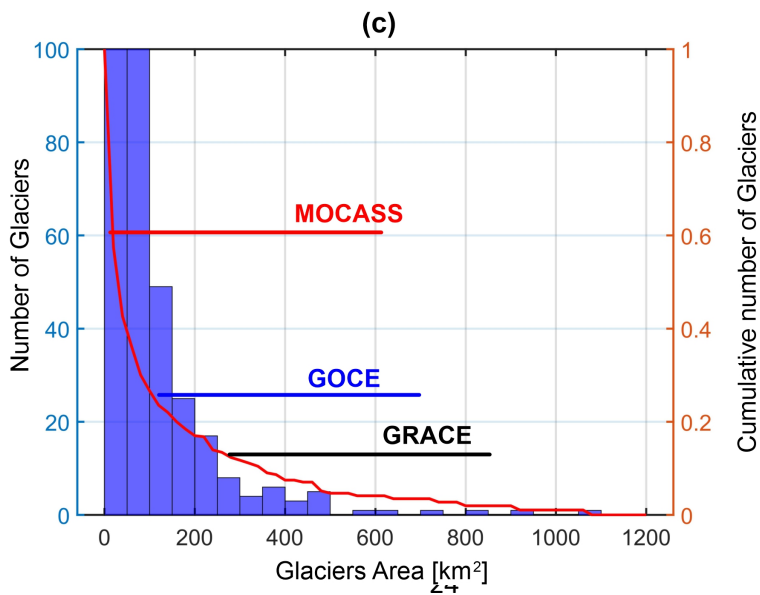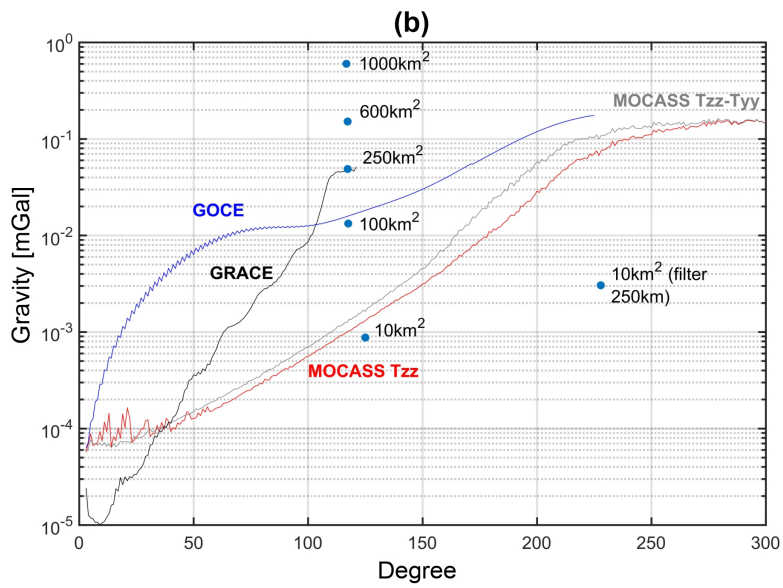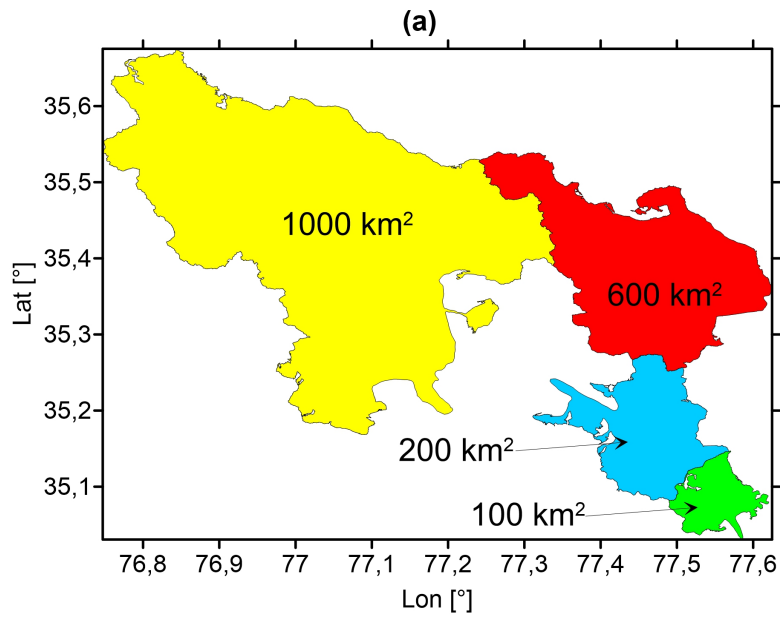
Figure 7. Gravity signal generated by the mass of different-sized glaciers in HMA. a) the location of the selected glaciers and their outline. b) gravity signal compared to error curves. The glacier height is estimated from the areal extension through an empirical formula. The signals are filtered with Gaussian low pass filter (500km cutoff wavelength). Only the small glacier with 10 km² is also filtered with 250 km. The error curves are for 5-year observation time. c) Statistical distribution of number of glaciers in HMA with respect to their size. The horizontal lines show the detectability ranges of the three satellites GRACE, GOCE and MOCASS. The first bin of the histogram reaches the value of 1900, the second about 700.

Considering the statistical distribution of the number of glaciers versus size, MOCASS achieves a significant step, because at sizes around 100 km^2 the number of smaller glaciers jumps significantly with respect to larger glaciers from 20 to 80 glaciers, as seen in Figure 7. With smaller areas, close to 100 km^2 the number of glaciers is 20 fold, which demonstrates that MOCASS achieves a very significant increase in glacier monitoring, because it crosses the border between copious and scarce number of glaciers, at least for the HMA. MOCASS covers therefore a much larger total mass of glaciers, including the small glaciers, against GOCE and GRACE, which catch the larger glaciers, but catch the signal of small glaciers only as aggregate signal, when the glaciers are close to each other and coalesce to one signal. Sparse and small glaciers are not observable by GOCE and GRACE.

5 Discussion and Conclusions

First estimates show that MOCASS brings significant improvement in the gravity field with respect to GRACE. An operational use of a satellite mission for glacier monitoring in mid-latitudes can presently not be made with GRACE because the resolution is too coarse. To catch 60% of the glacial areas in HMA a resolution of 100 km^2 is needed, provided by MOCASS. The signal would provide the mass loss of the integrated glaciated area, as well as the possibility to define present ice volumes starting from the glacier area detected from Sentinel 1 and 2, either through SAR or multispectral imaging.

Tectonic vertical movement is caught by GRACE, but the local anomalies, as in the Yunnan province, can only be caught with MOCASS. With gravity observations the geodynamic reasons for the subsidence can be distinguished, as tectonic stresses and sediment compaction.

561 For studying the hydrology of Tibet, only MOCASS can detect the predicted changes from the GLDAS,

562 as the observed reduction in moisture found in Eastern Tibet. In Eastern Tibet GRACE has a positive

563 gravity increase rate, that does not match the moisture decrease. Here the observed GRACE signal

564 probably contains the superposition of the tectonic and hydrologic mass change of opposite sign,

565 and the two effects cannot be resolved. A mission as MOCASS would allow to separate the two

566 hydrologic and tectonic effects in this strategic area.

567 In the Alps, where the hydrologic basins are much smaller ($4.5 \ 10^4$ km^2 Po Basin vs. $2.5 \ 10^6$ km^2 of

568 the Brahmaputra- Indus- Ganga systems), the resolution of GRACE is far from the expected signal,

569 and only MOCASS would allow to detect the hydrologic mass changes.

570 A further innovation with the MOCASS satellite would be the continuous monitoring of mass

571 changes at the top of sea mounts. The appearance of an uncharted ocean island is a rare event, due

572 to volcanic submarine activity. Although a rare event, in case of ship collision the risk is great, be it

573 ecological or of human loss. For submarine vehicles also the growth of a deep top of a seamount is

574 a danger, whereas for ships a shallow top is hazardous. The seamount with a shallow top below the

575 sea surface, is not observed from optical observations as obtained from Sentinel 2 or SAR

576 observations obtained from Sentinel 1. It may be detected from satellite altimetry, but the repeat

577 pass orbit has uncharted areas, in which a growing seamount could be fortuitously placed. The

578 MOCASS mission would detect a mass change of a seamount of 12 km radius, adding a volcanic mass

579 to the top of 10 m, which would result in a mass equal to the erupted volume of Mount Saint Helens.

580 The above examples have been tested in their first orders, and more study is required to underpin

581 the results before deciding on such a mission. One aspect to be studied in greater depth is the

582 method of comparing a local effect, as the one we have synthesized, with the global error curves

583 derived from spherical harmonic expansion. We propose to make a thorough study, both

584 transforming the local fields in the spectral space, as also comparing the local synthesized fields with

585 examples of noise simulations of the MOCASS satellite.

586 The further studies that could be made are an in depth study of the four geophysical phenomena

587 we have considered up to now, and the study of the added value of a gravity mission to detect the

588 different cycles of a seismogenic fault. In the following, we mention the further study that we think

589 is relevant for the phenomena discussed in this work.

590 Glaciosphere: investigate with which methods the glacier signal can be separated in the MOCASS

591 synthetics from the remainder gravity signal. Further, how the volume of a glacier can be effectively

592   determined given the digital terrain model which generally will give the top of the glacier surface,

593   and the outline of the glacier from Sentinel 1 and 2. Determine the effective ability of MOCASS to

594   be an operational satellite for glacier mass and glacier mass depletion detection in High Mountain

595   of Asia and other high mountain areas worldwide.

596   Hydrosphere: given the discrepancies between the predicted signal from the soil moisture models

597   and the direct observations of the underground water level from wells as shown in Chen et al. (2018)

598   the hydrologic model should be improved, so as to find a perfect match between GLDAS (moisture

599   model) and the wells observations of underground mass changes.

600   Sea mounts: we have demonstrated that a mass change on top of the sea mount is detectable, in

601   principle. The volcanic model should be improved, containing the volcanologic process of magma

602   eruption, to be sure that the mass erupted on the top is not just shifted upwards from the volcanic

603   edifice, but that effectively there is a mass change in the vertical column.

604   Our final conclusion is that the MOCASS mission has great potential for monitoring geophysical

605   phenomena, but that there is some more investigation needed to determine with high confidence

606   the applicability of the observed gravity field as a monitoring device.

607

608   **Declarations**

609   **Funding** The MOCASS study has been funded under Italian Space Agency contract N. 2016-9-U-0

610   Proposal of a satellite mission and sensor concept based on advanced atom interferometry

611   accelerometers for high resolution monitoring of mass variations on and below the Earth surface".

612   **Conflicts of interest/Competing interests.** None

613   **Availability of data and material** The data used in the study was retrieved on public databases, as

614   described in the manuscript.

615   **Code availability:** Calculations have been made with Custom codes.

616   *Author's contributions* CB was responsible and supervised the project, providing the main

617   conceptual ideas and following the project-stages. TP performed the coding, database retrieval and

618   simulations over the HMA region, DFB performed the simulations of the seamounts eruption. TP

619   and DFB compared the signals with the error curves of the gravity missions. All the authors discussed

620   the results of the simulations and assessed the impact of the mission.

621

629

630

631

632   **References**

633   Abe, M., Kroner, C., Förste, C., Petrovic, S., Barthelmes, F., Weise, A., et al. (2012). A comparison of

634   GRACE-derived temporal gravity variations with observations of six European

635   superconducting gravimeters: *Comparison of temporal gravity variations*. *Geophysical*

636   *Journal International*, *191*(2), 545–556. https://doi.org/10.1111/j.1365-246X.2012.05641.x

637   Amante, B., & Eakins, B. W. (2009). ETOPO1 1 arc-minute global relief model: procedures, data

638   sources and analysis. *NOAA Technical Memorandum NESDIS NGDC-24*.

639   https://doi.org/doi:10.7289/V5C8276M

640   Bahr, D. B., Pfeffer, W. T., & Kaser, G. (2015). A review of volume-area scaling of glaciers: Volume-

641   Area Scaling. *Reviews of Geophysics*, *53*(1), 95–140.

642   https://doi.org/10.1002/2014RG000470

643   Braitenberg, C. (2015). Exploration of tectonic structures with GOCE in Africa and across-

644   continents. *International Journal of Applied Earth Observation and Geoinformation*, *35*, 88–

645   95. https://doi.org/10.1016/j.jag.2014.01.013

646 Braitenberg, C., & Shum, C. K. (2017). Geodynamic implications of temporal gravity changes over

647   Tibetan Plateau. *Italian Journal of Geosciences*, *136*. https://doi.org/10.3301/IJG.2015.38

648 Cambiotti, G. (2020). Joint estimate of the co-seismic 2011 Tohoku earthquake fault slip and post-

649   seismic viscoelastic relaxation by GRACE data inversion. *Geophysical Journal International*,

650   *220*, 1012–1022. https://doi.org/10.1093/gji/ggz485

651 Carraz, O., Siemes, C., Massotti, L., Haagmans, R., & Silvestrin, P. (2014). A Spaceborne Gravity

652   Gradiometer Concept Based on Cold Atom Interferometers for Measuring Earth's Gravity

653   Field. *Microgravity Science and Technology*, *26*(3), 139–145.

654   https://doi.org/10.1007/s12217-014-9385-x

655 Chen, W., Braitenberg, C., & Serpelloni, E. (2018). Interference of tectonic signals in subsurface

656   hydrologic monitoring through gravity and GPS due to mountain building. *Global and*

657   *Planetary Change*, *167*, 148–159. https://doi.org/10.1016/j.gloplacha.2018.05.003

658 Colucci, R. R., & Žebre, M. (2016). Late Holocene evolution of glaciers in the southeastern Alps.

659   *Journal of Maps*, *12*(sup1), 289–299. https://doi.org/10.1080/17445647.2016.1203216

660 Döll, P., Müller Schmied, H., Schuh, C., Portmann, F. T., & Eicker, A. (2014). Global-scale

661   assessment of groundwater depletion and related groundwater abstractions: Combining

662   hydrological modeling with information from well observations and GRACE satellites.

663   *Water Resources Research*, *50*(7), 5698–5720. https://doi.org/10.1002/2014WR015595

664 Floberghagen, R., Fehringer, M., Lamarre, D., Muzi, D., Frommknecht, B., Steiger, C., et al. (2011).

665   Mission design, operation and exploitation of the gravity field and steady-state ocean

666   circulation explorer mission. *Journal of Geodesy*, *85*(11), 749–758.

667   https://doi.org/10.1007/s00190-011-0498-3

668 Fu, Y., & Freymueller, J. T. (2012). Seasonal and long-term vertical deformation in the Nepal

669   Himalaya constrained by GPS and GRACE measurements: GPS/GRACE vertical deformation

670   in Nepal. *Journal of Geophysical Research: Solid Earth*, *117*(B3).

671   https://doi.org/10.1029/2011JB008925

672 Gardner, A. S., Moholdt, G., Cogley, J. G., Wouters, B., Arendt, A. A., Wahr, J., et al. (2013). A

673   Reconciled Estimate of Glacier Contributions to Sea Level Rise: 2003 to 2009. *Science*,

674   *340*(6134), 852–857. https://doi.org/10.1126/science.1234532

675 Han, S. -C., Sauber, J., & Pollitz, F. (2015). Coseismic compression/dilatation and viscoelastic

676   uplift/subsidence following the 2012 Indian Ocean earthquakes quantified from satellite

677   gravity observations. *Geophysical Research Letters*, *42*(10), 3764–3772.

678   https://doi.org/10.1002/2015GL063819

679 Han, S.-C. (2006). Crustal Dilatation Observed by GRACE After the 2004 Sumatra-Andaman

680   Earthquake. *Science*, *313*(5787), 658–662. https://doi.org/10.1126/science.1128661

681 Han, S.-C., Yeo, I.-Y., Alsdorf, D., Bates, P., Boy, J.-P., Kim, H., et al. (2010). Movement of Amazon

682   surface water from time-variable satellite gravity measurements and implications for water

683   cycle parameters in land surface models. *Geochemistry Geophysics Geosystems*, *11*(9),

684   Q09007. https://doi.org/10.1029/2010GC003214

685 Jacob, T., Wahr, J., Pfeffer, W. T., & Swenson, S. (2012). Recent contributions of glaciers and ice

686   caps to sea level rise. *Nature*, *482*(7386), 514–518. https://doi.org/10.1038/nature10847

687 Jekeli, C. (1981). Alternative Methods to smooth the Earth's gravity field. *Report of the*

688   *Department of Geodetic Science and Surveying*, *Report No 327*, 54.

689 Jeon, T., Seo, K.-W., Youm, K., Chen, J., & Wilson, C. R. (2018). Global sea level change signatures

690   observed by GRACE satellite gravimetry. *Scientific Reports*, *8*(1), 13519.

691   https://doi.org/10.1038/s41598-018-31972-8

692 Köther, N., Götze, H.-J., Gutknecht, B. D., Jahr, T., Jentzsch, G., Lücke, O. H., et al. (2012). The

693   seismically active Andean and Central American margins: Can satellite gravity map

694   lithospheric structures? *Journal of Geodynamics*, *59–60*, 207–218.

695   https://doi.org/10.1016/j.jog.2011.11.004

696   Liang, S., Gan, W., Shen, C., Xiao, G., Liu, J., Chen, W., et al. (2013). Three-dimensional velocity field

697   of present-day crustal motion of the Tibetan Plateau derived from GPS measurements: 3-D

698   crustal motion within Tibetan plateau. *Journal of Geophysical Research: Solid Earth*,

699   *118*(10), 5722–5732. https://doi.org/10.1002/2013JB010503

700   Matsuo, K., & Heki, K. (2010). Time-variable ice loss in Asian high mountains from satellite

701   gravimetry. *Earth and Planetary Science Letters*, *290*(1–2), 30–36.

702   https://doi.org/10.1016/j.epsl.2009.11.053

703   Ménoret, V., Vermeulen, P., Le Moigne, N., Bonvalot, S., Bouyer, P., Landragin, A., & Desruelle, B.

704   (2018). Gravity measurements below 10−9 g with a transportable absolute quantum

705   gravimeter. *Scientific Reports*, *8*(1), 12300. https://doi.org/10.1038/s41598-018-30608-1

706   Migliaccio, F., Reguzzoni, M., Batsukh, K., Tino, G. M., Rosi, G., Sorrentino, F., et al. (2019).

707   MOCASS: A Satellite Mission Concept Using Cold Atom Interferometry for Measuring the

708   Earth Gravity Field. *Surveys in Geophysics*, *40*(5), 1029–1053.

709   https://doi.org/10.1007/s10712-019-09566-4

710   Mikolaj, M., Meurers, B., & Güntner, A. (2016). Modelling of global mass effects in hydrology,

711   atmosphere and oceans on surface gravity. *Computers & Geosciences*, *93*, 12–20.

712   https://doi.org/10.1016/j.cageo.2016.04.014

713   Pfeffer, W. T., Arendt, A. A., Bliss, A., Bolch, T., Cogley, J. G., Gardner, A. S., et al. (2014). The

714   Randolph Glacier Inventory: a globally complete inventory of glaciers. *Journal of*

715   *Glaciology*, *60*(221), 537–552. https://doi.org/10.3189/2014JoG13J176

716   Reguzzoni, M., Migliaccio, F., & Batsukh, K. (2021). Gravity field recovery and error analysis for the

717   MOCASS mission proposal based on cold atom interferometry. *Pure and Applied*

718   *Geophysics*, *under review*.

719   Rodell, M., Houser, P. R., Jambor, U., Gottschalck, J., Mitchell, K., Meng, C.-J., et al. (2004). The

720   Global Land Data Assimilation System. *Bulletin of the American Meteorological Society*,

721   *85*(3), 381–394. https://doi.org/10.1175/BAMS-85-3-381

722   Saji, A. P., Sunil, P. S., Sreejith, K. M., Gautam, P. K., Kumar, K. V., Ponraj, M., et al. (2020). Surface

723   Deformation and Influence of Hydrological Mass Over Himalaya and North India Revealed

724   From a Decade of Continuous GPS and GRACE Observations. *Journal of Geophysical*

725   *Research: Earth Surface*, *125*(1). https://doi.org/10.1029/2018JF004943

726   Sun, W., Wang, Q., Li, H., Wang, Y., Okubo, S., Shao, D., et al. (2009). Gravity and GPS

727   measurements reveal mass loss beneath the Tibetan Plateau: Geodetic evidence of

728   increasing crustal thickness: gravity reveals mass loss in Tibet. *Geophysical Research*

729   *Letters*, *36*(2), n/a-n/a. https://doi.org/10.1029/2008GL036512

730   Tapley, B. D., Watkins, M. M., Flechtner, F., Reigber, C., Bettadpur, S., Rodell, M., et al. (2019).

731   Contributions of GRACE to understanding climate change. *Nature Climate Change*, *9*(5),

732   358–369. https://doi.org/10.1038/s41558-019-0456-2

733   Uieda, L., Barbosa, V. C. F., & Braitenberg, C. (2016). Tesseroids: Forward-modeling gravitational

734   fields in spherical coordinates. *Geophysics*, *81*(5), F41–F48.

735   https://doi.org/10.1190/geo2015-0204.1

736   Weise, A., Kroner, C., Abe, M., Creutzfeldt, B., Förste, C., Güntner, A., et al. (2012). Tackling mass

737   redistribution phenomena by time-dependent GRACE- and terrestrial gravity observations.

738   *Journal of Geodynamics*, *59–60*, 82–91. https://doi.org/10.1016/j.jog.2011.11.003

739   Weise, A., Kroner, C., Abe, M., Ihde, J., Jentzsch, G., Naujoks, M., et al. (2009). Gravity field

740   variations from superconducting gravimeters for GRACE validation. *Journal of*

741   *Geodynamics*, *48*(3–5), 325–330. https://doi.org/10.1016/j.jog.2009.09.034

742   Wessel, P., Sandwell, D., & Kim, S.-S. (2010). The Global Seamount Census. *Oceanography*, *23*(01),

743   24–33. https://doi.org/10.5670/oceanog.2010.60

744   Yi, S., Freymueller, J. T., & Sun, W. (2016). How fast is the middle-lower crust flowing in eastern

745   Tibet? A constraint from geodetic observations: flow in eastern Tibet. *Journal of*

746   *Geophysical Research: Solid Earth*, *121*(9), 6903–6915.

747   https://doi.org/10.1002/2016JB013151

748   Zemp, M., Huss, M., Thibert, E., Eckert, N., McNabb, R., Huber, J., et al. (2019). Global glacier mass

749   changes and their contributions to sea-level rise from 1961 to 2016. *Nature*, *568*(7752),

750   382–386. https://doi.org/10.1038/s41586-019-1071-0

751   Zhang, G., Yao, T., Shum, C. K., Yi, S., Yang, K., Xie, H., et al. (2017). Lake volume and groundwater

752   storage variations in Tibetan Plateau's endorheic basin: Water Mass Balance in the TP.

753   *Geophysical Research Letters*, *44*(11), 5550–5560. https://doi.org/10.1002/2017GL073773

754

755

Supplementary material

758   Supplementary material shows the mass models employed for calculating the gravity signals in the

759   HMA region. Glaciers are responsible of spatially localized mass variations which can easily exceed

760   400 kg/m^2/yr, with peaks of 800 kg/m^2/yr. Tectonic and hydrologic linear trends show lower yearly

761   mass variations per unit area but widespread over large regions. Seasonal hydrologic mass

762   changes are dominant in the alluvial plains where they can exceed 200 kg/m^2; hence, mass

763   variations of the seasonal signal are one order of magnitude larger than long period components.
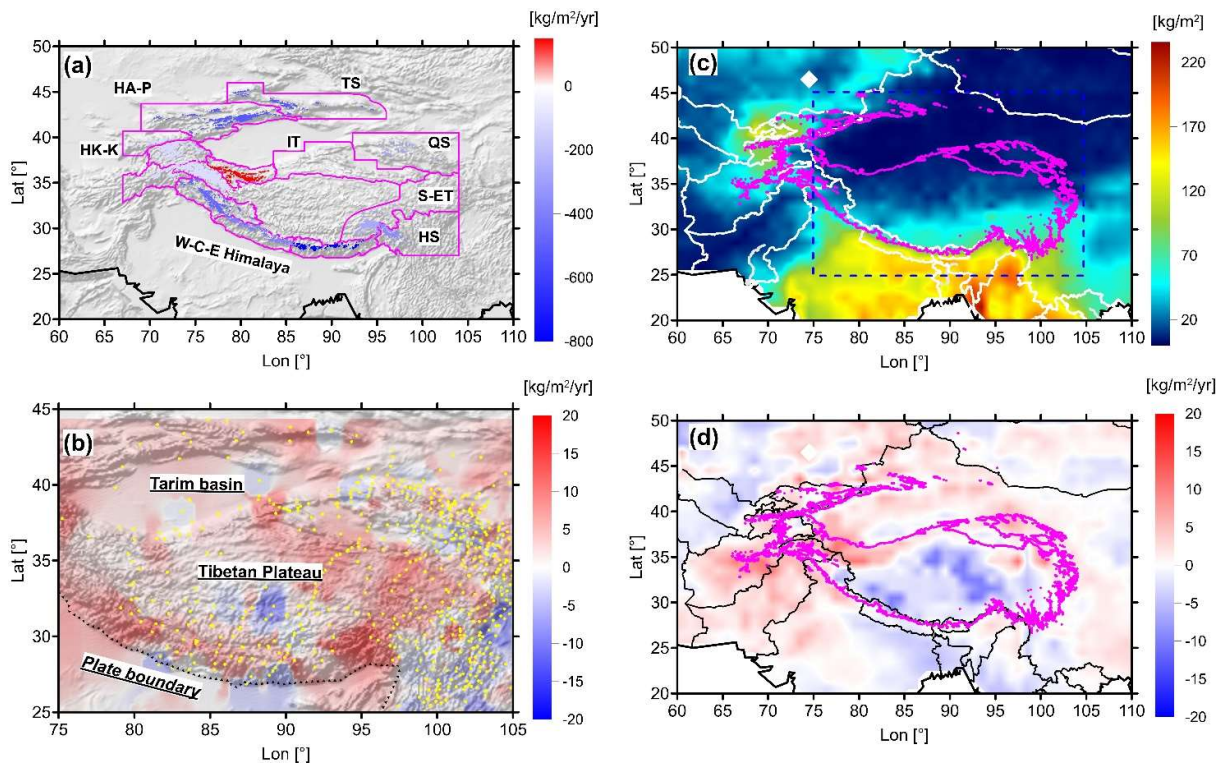
764

765   *Figure S1. Mass changes in the HMA region, reported in kg/m^2. a) mass change associated to the*

766   *glaciers in HMA. Purple outline reports the glacial sub-regions according to the RGI catalogue.*

767   *Labels are same as Figure 1a. In the background, the ETOPO1 hill-shade map. b) mass change*

768   *associated to vertical movements of the topography. Line with black triangles limits the plate*

769   *boundary between India and Eurasia. Yellow dots report GNSS measurement locations. In case the*

770   *isostatic response of the crust is assumed, the mass variations on the surface topography are*

771   *exactly counterbalanced at the Moho depth. In case of pure crustal uplift, we have a further mass*

772   *contribution at the Moho level which is around 1/5 of the superficial mass. In the background, the*

773   *ETOPO1 hill-shade map. c) Seasonal annual amplitude of the mass variations for the GLDAS*

774   *model. Black: coast line; white lines: national boundaries; purple contour line corresponding to*

775 *3500 m topography, bounding the Tibetan plateau region; dashed line shows the region where*

776 *tectonic mass changes are calculated (plot S1b) d) long term mass variations of the GLDAS model;*

777 *black outlines: coastline and national boundaries; purple: contour line corresponding to 3500 m.*